Cobalt promoted TiO$_2$/GO for the photocatalytic degradation of oxytetracycline and Congo Red

Wan-Kuen Jo[a], Santosh Kumar[b], Mark. A. Isaacs[b], Adam F. Lee[b], S. Karthikeyan[a,b,*]

[a] Department of Environmental Engineering, Kyungpook National University, Daegu 702-701, South Korea
[b] European Bioenergy Research Institute, Aston University, Aston Triangle, Birmingham B4 7ET, United Kingdom

ARTICLE INFO

ABSTRACT

A family of titania derived nanocomposites synthesized via sol-gel and hydrothermal routes exhibit excellent performance for the photocatalytic degradation of two important exemplar water pollutants, oxytetracycline and Congo Red. Low loadings of Co$_3$O$_4$ nanoparticles dispersed over the surfaces of anatase TiO$_2$ confer visible light photoactivity for the aqueous phase decomposition of organics through the resulting heterojunction and reduced band gap. Subsequent modification of these Co$_3$O$_4$/TiO$_2$ composites by trace amounts of graphene oxide nanosheets in the presence of a diamine linker further promotes both oxytetracycline and Congo Red photodegradation under simulated solar and visible irradiation, through a combination of enhanced photoresponse and consequent radical generation. Radical quenching and fluorescence experiments implicate holes and hydroxyl radicals as the respective primary and secondary active species responsible for oxidative photodegradation of pollutants.

1. Introduction

Heterogeneous semiconductor photocatalysts have received significant attention owing to their potential application in a wide range of photoinduced reactions, notably photocatalytic hydrogen production, removal of organic contaminants and air pollutants, and electricity production using solar cells [1–4]. TiO$_2$ has historically been used for the removal of water pollutants because of its high photocatalytic efficiency, stability, and non-toxicity [5]. The surfaces of TiO$_2$ photocatalysts can be extremely hydrophilic, with a water contact angle of 0° [6] when activated by ultraviolet (UV) irradiation during photocatalytic and photoinduced oxidation processes [7]. However, as a wide band gap semiconductor (~3.2 eV), the requirement by TiO$_2$ for UV irradiation results in a low solar quantum efficiency and a high recombination rate for electron-hole pairs, limiting its practical utility [8]. Promotion by various transition metals (e.g. Pt, Ru, Ag, Rh, Au and Pd) [9–12] and transition metal oxides (e.g. Co$_3$O$_4$, CoO, Cu$_2$O, and α-Fe$_2$O$_3$) [13–17] has therefore been pursued as a means to generate visible light photoactivity in titanias, hinder charge carrier recombination, and to improve product selectivity [18,19].

Heterojunctions between metals and semiconducting materials are a proven strategy to suppress the recombination of photo-generated electrons and holes in TiO$_2$ [20], and to extend photon absorption (via e.g. plasmonic effects reference) into the visible regime. However, the high cost and scarcity of noble metals hinders their use in large scale applications such as water purification. Metal oxide promoted semiconductor photocatalysts have also shown promise in the oxidative degradation of organic compounds in aqueous solution [21], offering low cost and earth abundant components to meet photocatalytic applications [22,23].

Cobalt oxides have received attention because of their enhanced photocatalytic activity in CO$_2$ reduction under visible light and in oxygen reduction, depollution technologies, and also in dye-sensitized solar cells for power generation [24–26]. Cobalt oxide is therefore an interesting earth abundant mineral for producing visible light titania photocatalysts [27]. Nitrogen-doped graphene and graphene oxide (GO) have attracted interest as a substrate facilitating the uniform distribution of heterojunction materials [22] and enhanced photocatalytic activity through charge separation and transport [28]. Cobalt oxide promoted TiO$_2$ supported on reduced GO was recently reported as a visible light phottcatalyst for aqueous phase 2-chlorophenol photo-degradation [29–32].

Here we explore the potential impact of Co$_3$O$_4$/TiO$_2$/GO photocatalysts under solar/visible light for the degradation of oxytetracycline (OTC) and Congo Red (CR) in aqueous solution. OTC and CR, which exemplify organic contaminants introduced

* Corresponding author at: European Bioenergy Research Institute, Aston University, Aston Triangle, Birmingham B4 7ET, United Kingdom.
E-mail addresses: sekark@aston.ac.uk, catalkarthik1985@gmail.com (S. Karthikeyan).

into the aquatic environment [33,34] from industrial pharmaceutical and textile processes, are potentially carcinogenic, highly toxic, and have mutagenic properties. Here we want to demonstrate the utilisty/verstatility of CO/TiO2/GO composite towards the degradation of a variety of important organic pollutants. This work presents novel spinel-like photocatalysts, with notable Co_3O_4 coordination environments and oxidation states, for oxidation under solar/visible light, thus offering an ecologically and economically viable technology for the removal of toxic organic compounds from industrial wastewater. The mechanism underlying the oxidative degradation of OTC and CR by spinel-like Co_3O_4-TiO_2/GO photocatalysts under visible light is also proposed.

2. Materials and methods

2.1. Synthesis of cobalt-promoted TiO_2 catalysts

Cobalt-titanium mixed metal oxides were prepared by a sol-gel synthesis in which 0.4 mol cobalt nitrate ($Co(NO_3)_2 \cdot 6H_2O$, 98%) was dissolved in 50 mL deionized H_2O, prior to the addition of 50 mL of a solution of 0.013 mol titanium isopropoxide ($C_{12}H_{28}O_4Ti$, 97%) in ethanol. The resulting orange mixture was stirred for 4 h, followed by ultrasonication for 3 h to yield a solid which was subsequently air dried for 24 h and then in an oven at 70 °C overnight to remove solvents, and calcined at 400 °C for 2 h. The resulting composite was washed with deionized water and dried in vacuo at 60 °C for 5 h and the final solids labelled as X wt% Co_3O_4/TiO_2, with the quantity of cobalt nitrate precursor varied to obtain titanias with different cobalt loading. Nominal loadings are reported throughout, with actual loadings given in Table S1.

2.2. Synthesis of amine functionalized Co_3O_4/TiO_2/GO composites

A modified Hummers method [35] was used to synthesize GO from ordinary graphite powder (>20 μm, Sigma). 0.2 mg of the resulting GO was dispersed in 100 mL ethanol through 30 min ultrasonication. Cobalt-titanium mixed metal oxide was introduced to the GO suspension, followed by the addition of 2 mL ethane-1,2-diamine ($C_2H_5(NH_2)_2$, 99%) as a linking agent to enhance metal oxide dispersion across the GO; this mixture was subsequently stirred for 8 h at 60 °C. This suspension was then ultrasonicated for 4 h prior to heating in a Teflon-lined autoclave at 200 °C for 6 h under an inert atmosphere to yield a greenish-black solid which was filtered and washed five times with deionized H_2O and ethanol, and then dried in vacuo at 70 °C for 6 h. The final composite powders were labelled amine functionalized 2 wt% Co_3O_4/TiO_2/GO-X with the mass of GO varied to obtain composites with different loadings.

2.3. Catalyst characterization

Crystallinity and phase analysis was performed by powder X-ray diffraction (XRD) using a Rigaku X-Ray diffractometer (D/Max-2500) with Cu Kα_1 radiation ($\lambda = 0.154059$ nm) over $2\theta = 5$–$80°$ at $3°$ min^{-1} and 40 kV and 200 mA. X-ray photoelectron spectroscopy (XPS) was performed on a ULVAC-PHI Quantera SXM^{TM} scanning XPS microscope with Al Kα radiation source or a Kratos Axis HSi photoelectron spectrometer equipped with a charge neutralizer and monochromated Al Kα (1486.6 eV) radiation. Spectra were fitted using CasaXPS version 2.3.14. Binding energies were corrected to the C 1s peak at 284.6 eV and surface atomic compositions calculated via correction for the appropriate instrument response factors. Diffuse reflectance UV–vis spectroscopy (DRUVS) was employed using a Shimadzu UV-2600 spectrophotometer to determine band gaps over the wavelength range 200–800 nm with

a barium sulfate ($BaSO_4$) as a standard reference material. Band gaps were calculated using Eq. (1) [36–38]:

$$\alpha h\nu = A\left(h\nu - E_g\right)^{\eta} \tag{1}$$

where α, $h\nu$, E_g and A are absorption coefficient, light frequency, band gap, and a proportionality constant respectively, and variable η depends on the nature of the optical transition during photon absorption. For indirect band gap materials such as anatase TiO_2 and Co_3O_4, E_g can be estimated from a Tauc plot of $(\alpha h\nu)^{0.5}$ versus $h\nu$, with the optical absorption coefficient obtained from the Kubelka–Munk function obtained from Eq. (2) below, by fitting a tangent to the band edge as shown in Fig. 4:

$$\alpha = \frac{(1-R)^2}{2R} \tag{2}$$

Nanostructures were visualized by high-resolution transmission electron microscopopy (HR-TEM) on a FEI Titan G2 ChemiSTEM Cs Probe microscope. Samples were prepared through dispersion in ethanol and dropwise application to a carbon coated copper grid. Surface morphology was also visualized by a Hitachi SU8220 field emission scanning electron microscope (FE-SEM), and compositions by a HORIBA X-Max^N energy-dispersive X-ray spectroscopy (EDS) system equipped with a silicon DRIFT X-ray detector. Samples were mounted on an aluminum stub using silver paint, after which a platinum coating was applied by ion sputtering (Hitachi, E-1030) for 60 s. Textural properties were characterized by nitrogen porosimetry on a BET-BELSORP Mini II surface area analyzer, to calculate pore size distributions and BET surface areas.

Photocurrent measurements were performed on an electrochemical analyzer in a standard three-electrode system by using the films of the samples as the working electrode, and a platinum (Pt) coil and saturated calomel electrode (SCE) as the counter and reference electrodes. Working electrodes of composites were prepared by grinding 0.5 g in a mortar and pestle and 0.5 mL ethanol to form a slurry which was then coated on indium-tin oxide (ITO) glass by the doctor blade method, prior to calcination at 300 °C for 1 h. Aqueous 0.1 M Na_2SO_4 solution was used as the electrolyte. Photocurrents were measured under visible light irradiation using a variety of on/off irradiation cycles. Diffuse reflectance IR spectroscopy (DRIFTS) was performed on a Perkin-Elmer Frontier spectrophotometer between 400 and 4000 cm^{-1} for samples diluted in KBr. UV–Vis absorption spectra of OCT and CR were recorded between 200 and 800 nm on a Shimadzu UV-2600 spectrophotometer. Liquid chromatography/tandem mass spectrometry (LC/MS/MS) analysis was undertaken to identify products of CR and OCT photodegradation. A Dionex Ultimate 3000 HPLC and Thermo Scientific TSQ Quantiva Triple-quadrupole mass spectrometer system were used for LC separation and mass detection, respectively. LC separation was performed on a C18 Hypersil GOLD column (50×2.1 mm) and mass detection was performed in the positive mode of an atmospheric pressure chemical ionization (APCI) process. Elemental analysis of Co_3O_4/TiO_2/GO catalysts before and after CR and OTC oxidation employed a Perkin Elmer Optima 5300 DV ICP-OES instrument.

2.4. Photocatalytic oxidation of OTC and CR by amine functionalized Co_3O_4/TiO_2/GO

Photocatalytic efficiencies of commercial reference and composite catalysts were measured for OCT and CR photodegradation under visible/solar light sources using a bespoke borosilicate reactor [39]. For photocatalytic oxidation, aqueous OTC and CR (200 mL, 10 mg L^{-1}) and 50 mg catalyst were added to the reactor and stirred for 30 min in the dark to equilibrate adsorption processes. The reactor was then illuminated by a 300 W Xe solar simulator (spectral distribution of the light source is presented in Fig. S1) equipped
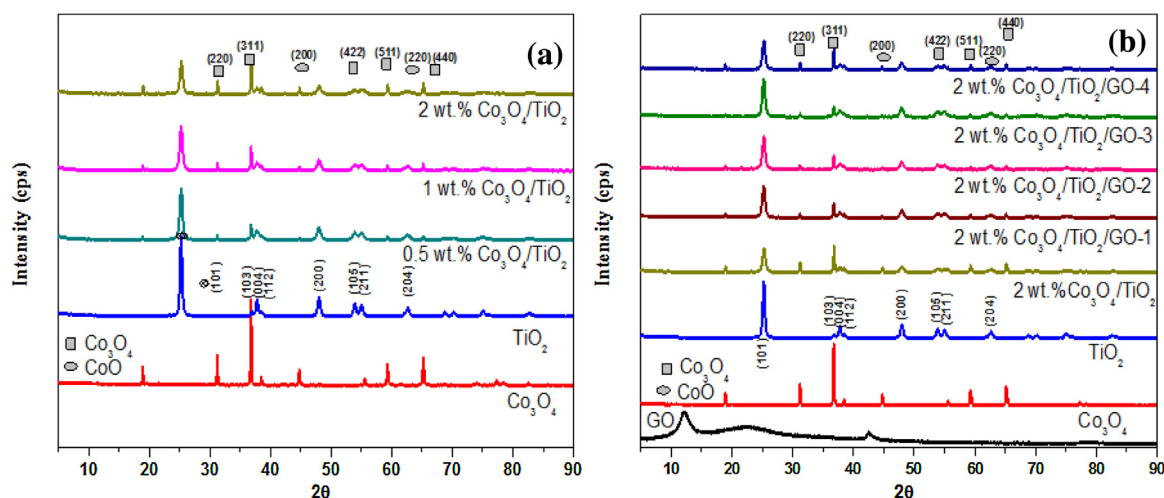
Fig. 1. Powder XRD diffractograms of (a) Co_3O_4/TiO_2 and (b) amine funtionalized 2 wt% $Co_3O_4/TiO_2/GO$ nanocomposites as a function of Co or GO loading. Reference Co_3O_4, anatase and GO standards are shown for comparison.

with a water filter to remove infrared radiation, and removable 400 nm cut-off filter to remove UV radiation; light intensity within the photoreactor was 100 mW cm^{-2}. The photoreactor was cooled with re-circulating water throughout the reaction while agitation was maintained. Aliquots (8 mL) aliquots were withdrawn periodically for UV–vis analysis. Post-reaction, photocatalysts were separated from the aqueous solution by centrifugation (6000 rpm, 15 min) prior to UV–vis analysis. The degree of OTC and CR removal was quantified from calibration curves constructed from their standards.

2.5. Fluorescence analysis of hydroxyl radical generation

The photocatalytic efficacy of the 2 wt% $Co_3O_4/TiO_2/GO$-1 nanocomposite was evaluated by assaying in situ hydroxyl radical generation. Generation of OH$^\bullet$ radicals was determined with terephthalic acid (TA) via fluorescence spectroscopy with a visible/solar light source; terephthalic acid reacts with hydroxyl radicals to form 2-hydroxyterephthalic acid (2-HTA), a strongly fluorescent molecule. Fluorescence analysis was performed using the same procedure as photocatalytic oxidation, but substituting the

organic pollutants for TA (5×10^{-4} M) in dilute sodium hydroxide solution (2×10^{-3} M). The reaction mixture was irradiated with solar/visible light, and the 2-HTA ($\lambda = 425$–432 nm emission) product quantified using a Shimadzu RF-6000PC spectrofluorophotometer with the excitation wavelength fixed at 315 nm.

2.6. Detection of reactive species

Electrons (e_{cb}^-), holes (h_{vb}^+), hydroxyl radicals ($^\bullet$OH), and superoxide radical anions ($O_2^{\bullet -}$) are known to cause oxidative degradation/reduction of our organic pollutants. Information on such reactive species, which may be rate-controlling in CR and OTC oxidation was therefore undertaken using radical trapping agents such as C_3H_8O (IPA, 10 mmol L^{-1}), $C_6H_4O_2$ (BQ, 0.1 mmol/L) and (NH4)2C2O4 (AO, 6 mmol L^{-1}) during the photocatalytic reactions. The trapping protocol was the same as for photocatalytic oxidation, but with the trapping agents added to the reaction mixture prior to the photocatalyst.
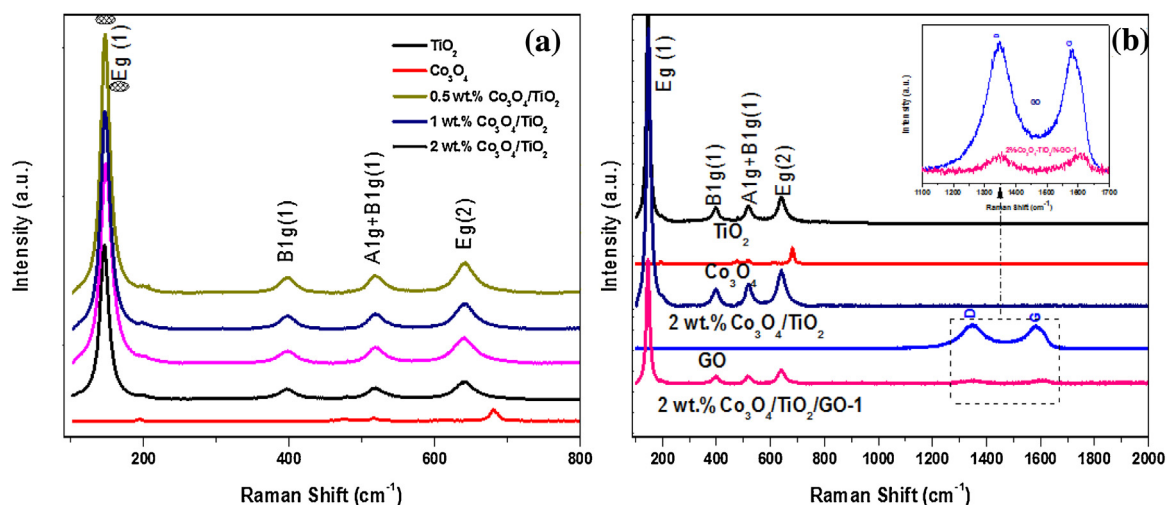

Fig. 2. (a) Raman spectra of (a) Co_3O_4/TiO_2 and (b) amine functionalized 2 wt% $Co_3O_4/TiO_2/GO$ nanocomposites as a function of Co or GO loading. Reference Co_3O_4, anatase and GO standards are shown for comparison.

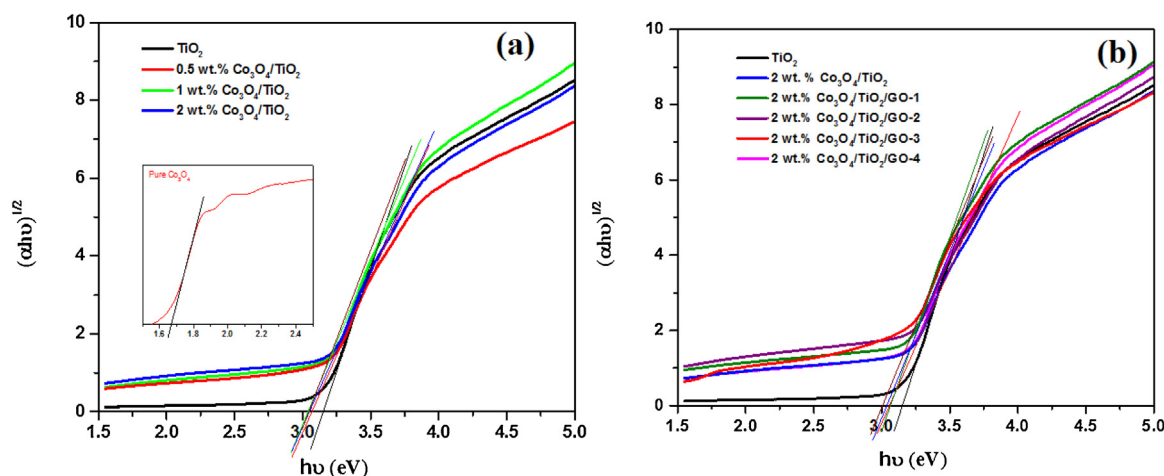**Fig. 3.** Tauc plots of (a) Co_3O_4/TiO_2 and (b) amine functionalized 2 wt% $Co_3O_4/TiO_2/GO$ nanocomposites as a function of Co or GO loading. Reference anatase standard is shown for comparison.

3. Results and discussion

3.1. Powder X-ray diffraction

Powder XRD patterns for the Co_3O_4/TiO_2 and $Co_3O_4/TiO_2/GO$ nanocomposites are shown in Fig. 1. The Co_3O_4/TiO_2 materials all exhibited reflections at $2\theta = 25.6, 36.8, 37.62, 38.57, 48.24, 53.96, 55.75, 62.46, 68.48, 71.01$ and $75.12°$ characteristic of the (101), (103), (004), (112), (200), (105), (211), (213), (116) and (220) planes respectively of anatase TiO_2 (JCPDS-00-021-1272). Additional reflections were also observed in all cases at $2\theta = 18.98°$, $31.32°, 36.71°, 38.49°, 44.75°, 59.34°$ and $66.18°$ corresponding to the respective (111), (220), (311), (222), (400), (511) and (440) planes of cubic Co_3O_4 (JCPD 78-1970), and weaker reflections at (200) and (220) associated with CoO (JCPDS 43-1004) [40], evidencing phase separation from the titania. There was also no observable shift in any of the titania reflections following Co addition. These findings demonstrate that Co was not substituted into the titania lattice, but rather present as a discrete (predominantly) Co_3O_4 phase dispersed over the TiO_2 surface.

Diffractograms of the amine functionalized 2 wt% $Co_3O_4/TiO_2/GO$ nanocomposites were essentially identical to those of the 2 wt% Co_3O_4/TiO_2 material, indicating negligible perturbation of the component Co_3O_4 or TiO_2 phases by either ethane-1,2-diamine or GO. The absence of GO features likely reflects the low dimensionality and/or size of the GO component; the XRD pattern of the parent GO exhibited a reflection at $2\theta = 12.16°$ attributed to the presence of oxygen functional groups [41].

3.2. Raman spectra

Raman spectroscopy is a powerful tool for characterizing metal oxides and graphene oxide. Fig. 2a shows the Raman spectra of as-prepared Co_3O_4/TiO_2 composites. Pure anatase exhibits Raman bands at 147, 395, 517, and 638 cm^{-1} associated with Eg, B1g, A1g or B1g, and Eg vibrations [42], all of which were also observed in the synthetic Co_3O_4/TiO_2 composites, indicating that titania was present as anatase within these. None of the anatase features showed appreciable shifts relative to pure anatase, indicating negligible Co lattice substitution. However, no bands attributable to cobalt oxide phases were apparent, likely a combination of the weak intensities of Co_3O_4 and due to the low Co loadings in the composites. Incorporation of GO into the Co_3O_4/TiO_2 nanocomposite resulted in the appearance of two new, weak features at

1358 cm^{-1} and 1600 cm^{-1} characteristic of the 'D' and 'G' bands of GO respectively (Fig. 2b) [43].

3.3. Diffuse reflectance UV–Vis

Fig. 3 shows Tauc plots of Co_3O_4/TiO_2 and amine functionalized $Co_3O_4/TiO_2/GO$ composites obtained from DRUV spectra (Fig. S2). Co addition decreased the indirect band gap of the Co_3O_4/TiO_2 composites relative to pure anatase [44] from 3.15 to 3.03 eV (Table 1).

3.4. Porosimetry

Textural properties of the as-prepared samples were investigated by nitrogen porosimetry (Fig. S3). The N_2 adsorption-desorption isotherms of all Co_3O_4/TiO_2 and amine functionalized 2 wt% $Co_3O_4/TiO_2/GO$ nanocomposites displayed type II isotherms with H3 hysteresis loops indicative of low porosity materials possessing a wide mesopore distribution and slit and/or panel-shaped mesopores [45]. Corresponding BET surface areas and total pore volumes are shown in Table 1. Co addition resulted in a small decrease in both surface area and pore volume for the Co_3O_4/TiO_2 materials, possibly due to the loss of intra-particle mesopore voids between anatase crystallites [46]. GO addition to the 2 wt% Co_3O_4/TiO_2 partially reversed these losses, reflecting the high area of the former (around 740 m^2 g^{-1}).

3.5. X-ray photoelectron spectroscopy

Surface elemental analysis of Co_3O_4/TiO_2 and amine functionalized 2 wt% $Co_3O_4/TiO_2/GO$ nanocomposites is reported in Table S1,

Table 1
Textural properties and band gaps of Co_3O_4/TiO_2 and amine functionalized 2 wt% $Co_3O_4/TiO_2/GO$ nanocomposites.

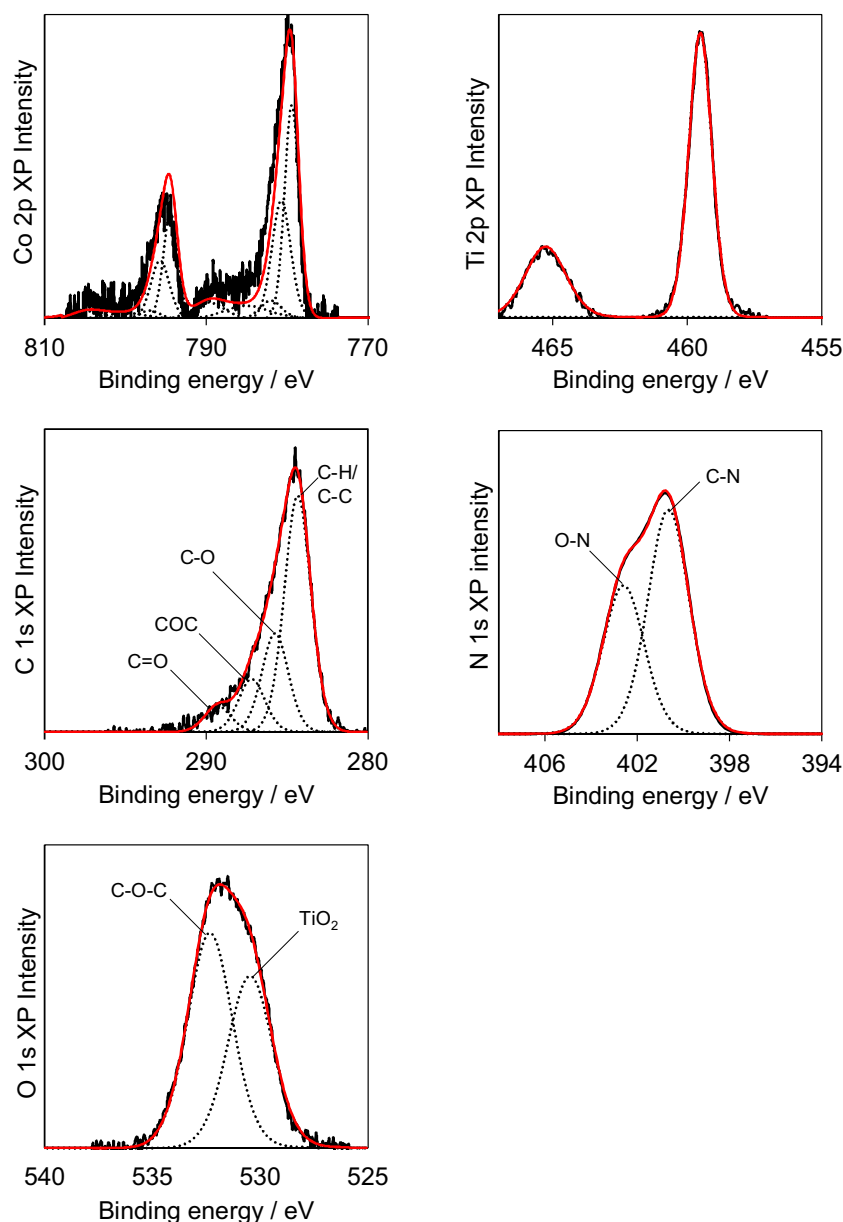| Photocatalyst	BET surface area/m^2 g^{-1}	Total pore volume/cm^3 g^{-1}	Band gap/eV[a]
TiO_2 reference	79	0.284	3.15
Co_3O_4 reference	0.5	0.004	1.70
0.5 wt% Co_3O_4/TiO_2	78	0.296	3.07
1 wt% Co_3O_4/TiO_2	73	0.266	3.04
2 wt% Co_3O_4/TiO_2	57	0.250	3.04
2 wt% Co_3O_4/TiO_2/GO-1	65	0.240	3.05
2 wt% Co_3O_4/TiO_2/GO-2	67	0.247	3.05
2 wt% Co_3O_4/TiO_2/GO-3	68	0.246	3.04
2 wt% Co_3O_4/TiO_2/GO-4	68	0.243	3.03

[a] Calculated from Eq. (1).

Fig. 4. High-resolution Co and Ti 2p, and C, O and N 1 s XP spectra of amine functionalized 2 wt% Co_3O_4/TiO_2/GO-1.

and high-resolution Co 2p, Ti 2p, C 1s, N 1s and O 1s XP spectra are shown in Fig. 4. Co 2p spectra were fitted adopting the procedure reported by Biesinger et al. [47] for Co_3O_4. A good fit to the main Co $2p_{3/2}$ state centered at 779.9 eV binding energy was obtained using previously published spin-orbit split multiplets consistent with the presence of Co_3O_4. [48] The Co 2p binding energy and lineshape was independent of Co loading, and/or GO indicating a common surface species in all cases. The Ti 2p XP spectra of all composites were consistent with TiO_2 (Ti $2p_{3/2}$ spin-orbit component at 459.5 eV) and independent of modification by Co or GO. C 1s XP spectrum of the amine functionalized 2 wt% Co_3O_4/TiO_2/GO-1 material revealed a range of distinct chemical environments associated with C=O (289.2 eV), C—O—C (287 eV), C—OH (286 eV), and C—C/C—H (284.5 eV) functional groups, consistent with literature reports for graphene oxide [49]. The N 1s XP spectrum of the ternary composite revealed two chemical states, consistent with N—C (400.8 eV) and N—O (402.7) environments present in the anticipated amide function resulting from hydrolysis of the diamine linker during hydrothermal processing of Co_3O_4/TiO_2 in the

presence of GO. The total surface N concentration was only ~0.7 wt%, consistent with the formation of a small number of surface amide linkers at the interfaces between Co_3O_4 and/or GO and/or TiO_2 components.

3.6. DRIFTS

DRIFT spectra of Co_3O_4/TiO_2 and amine functionalized Co_3O_4/TiO_2/GO composites are shown in Fig. S4. All the materials exhibited absorption peaks between 3497 and 3352 cm^{-1} associated with surface hydroxyls. The Co_3O_4/TiO_2/GO-X composites also displayed strong peaks around 1515 cm^{-1} and 1622 cm^{-1} indicative of amide functional groups formed following amine functionalization and hydrothermal processing. The band observed at 1320 cm^{-1} may arise from Ti-O-C linkages [11] in the amine functionalized Co_3O_4/TiO_2/GO composites, while those spanning 714–571 cm^{-1} are due to the TiO_2 and Co_3O_4 components [50], supporting the presence of separate oxide phases and possibility of heterojunction formation.
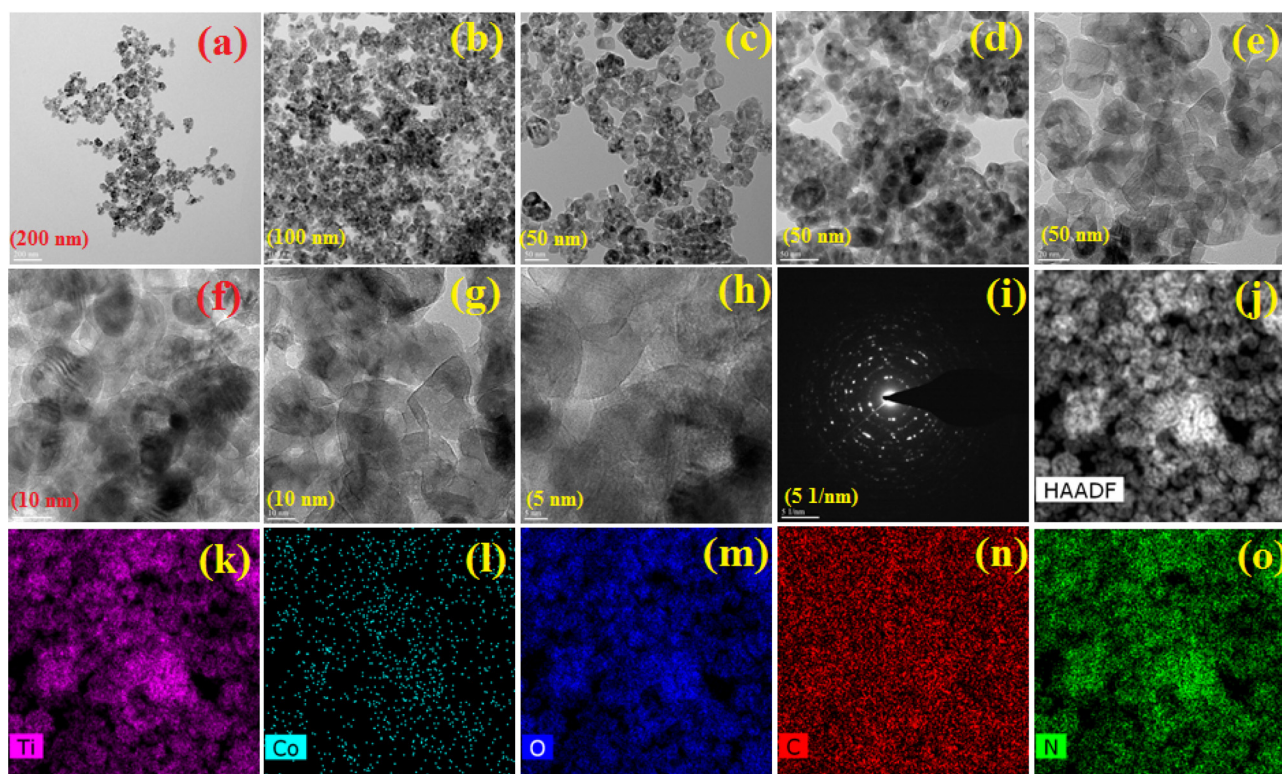
Fig. 5. (a-h) HR-TEM micrographs, (i) corresponding SAED pattern and (j-o) HAADF-(S)TEM image and elemental mapping of amine functionalized 2 wt% $Co_3O_4/TiO_2/GO$ composite.

3.7. Transmission electron microscopy

HR-TEM images of 2 wt% $Co_3O_4/TiO_2/GO$ composites (Fig. 5a–h) were dominated by approximately spherical 30–50 nm TiO_2 crystallites (in accordance with SEM, Fig. S5). Elemental mapping confirmed a uniform distribution of Co, C and N, from respective Co_3O_4, GO and amine components, across the anatase nanoparticles. Lattice fringes of 0.468 nm and 0.243 nm characteristic of respective (111) and (311) planes of Co_3O_4 were observed (Fig. S6a–f), in accordance with XRD analysis, associated with nanoparticles of 2–8 nm diameter, in contact with titania.

3.8. Photocatalytic oxidation of OTC and CR

The photocatalytic performance the Co_3O_4/TiO_2 and $Co_3O_4/TiO_2/GO$ nanocomposites was explored for OTC and CR degradation under simulated solar irradiation, and expressed as the resulting removal efficiency in Fig. 6a–d derived from UV–Vis analysis of the reaction mixture. In all cases, the Co_3O_4/TiO_2 composite significantly outperformed either pure metal oxide,

despite the low Co loadings introduced, reaching a maximum at 2 wt% Co for both pollutants, possibly due to partial encapsulation of the underlying titania by Co_3O_4, hindering light absorption by the former [51]. Reactions followed pseudo-first order kinetics, and initial rates determined from the linear portion of the reaction profiles are reported in Table 2. The incorporation of GO into the 2 wt% Co_3O_4/TiO_2 composite imparted a modest enhancement of ~15–20% in photocatalytic degradation of CR and OTC, with a maximum attained for 3–4 wt% GO addition.

Pohotcatalytic performance of the amine functionalized 2 wt% $Co_3O_4/TiO_2/GO$-1 composite was compared under simulated solar versus visible light irradiation (Fig. S7), which reveals that around 60% of the observed photoactivity for CR arises from visible light excitation (i.e. not direct UV photoexcitation of titania), consistent with Fig. 6d.

The superior activity of the Co_3O_4/TiO_2 composites is ascribed to the presence of heterojunctions and associated charge transport between Co_3O_4 and TiO_2 components, which likely suppresses charge recombination. GO incorporation may promote additional photoinduced charge carrier separation. The percentage

Table 2
Photodegradation of OCT and CR under simulated solar irradiation by Co_3O_4/TiO_2 and amine functionalized 2 wt% $Co_3O_4/TiO_2/GO$ photocatalysts.

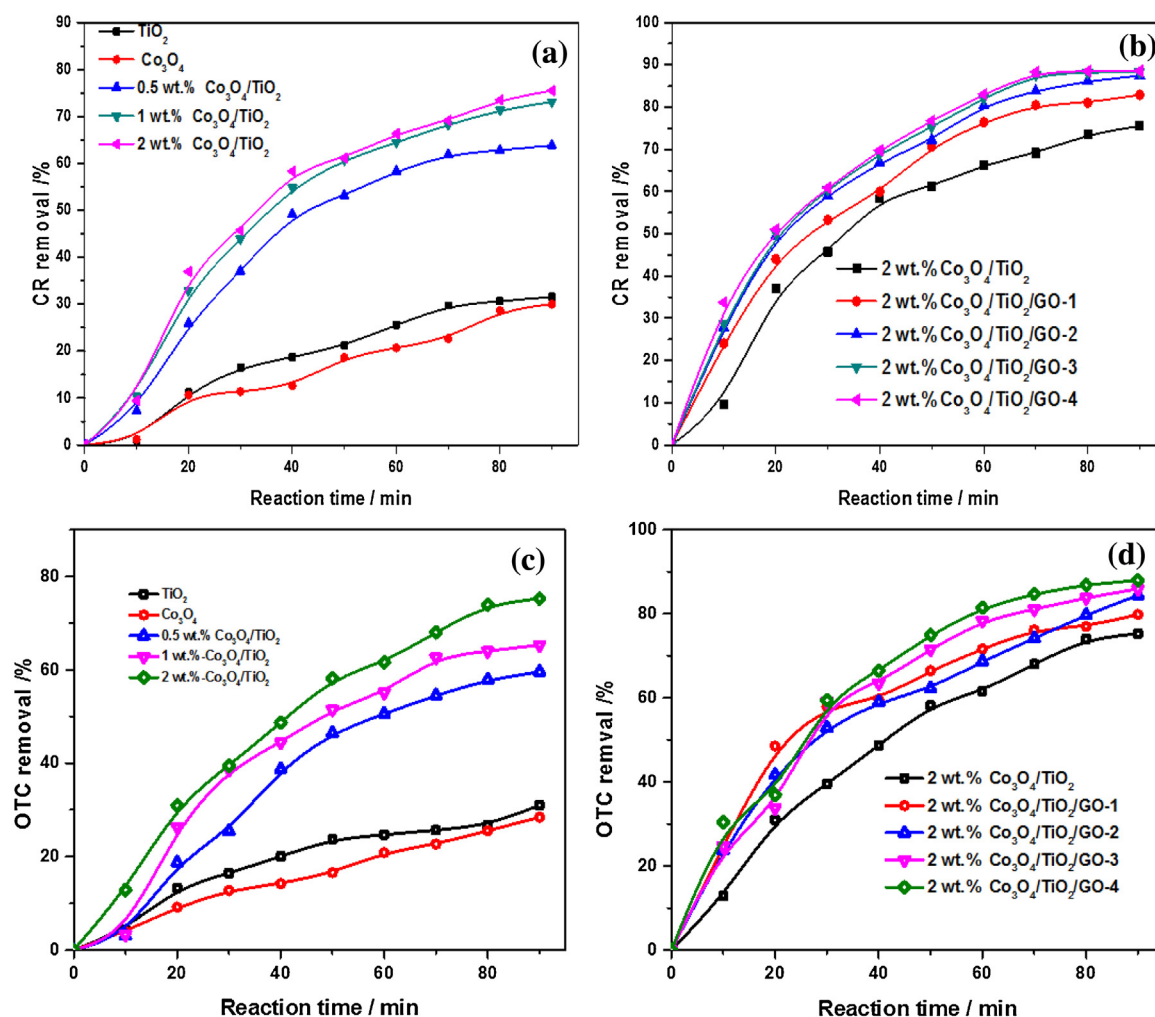| Photocatalyst	OTC		CR	
	Initial rate/mmol min^{-1} g$^{-1}_{cat}$	k/min^{-1}	Initial rate/mmol min^{-1} g$^{-1}_{cat}$	k/min^{-1}
TiO_2 reference	2.4×10^{-3}	0.0058	1.6×10^{-3}	0.0053
Co_3O_4 reference	1.8×10^{-3}	0.0040	1.6×10^{-3}	0.0040
0.5 wt% Co_3O_4/TiO_2	3.7×10^{-3}	0.0124	3.5×10^{-3}	0.0165
1 wt% Co_3O_4/TiO_2	5.6×10^{-3}	0.0163	4.2×10^{-3}	0.0198
2 wt% Co_3O_4/TiO_2	5.7×10^{-3}	0.0170	4.4×10^{-3}	0.0206
2 wt% $Co_3O_4/TiO_2/GO$-1	8.3×10^{-3}	0.0226	4.7×10^{-3}	0.0235
2 wt% $Co_3O_4/TiO_2/GO$-2	$8.6 10^{-3}$	0.0239	5.8×10^{-3}	0.0256
2 wt% $Co_3O_4/TiO_2/GO$-3	8.5×10^{-3}	0.0262	5.1×10^{-3}	0.0277
2 wt% $Co_3O_4/TiO_2/GO$-4	8.3×10^{-3}	0.0272	4.0×10^{-3}	0.0282

Fig. 6. Photodegradation of (a-b) CR and (c-d) OTC under simulated solar irradiation over Co_3O_4/TiO_2 and amine functionalized 2 wt% $Co_3O_4/TiO_2/GO$ nanocomposites determined by UV–Vis.

degradation was slightly larger than when using visible-light irradiation, perhaps due to the simulated solar light wavelength ranging from 311 to 600 nm and the visible light source ranging from 420 to 600 nm. The present catalytic system (heterogeneous nanocomposite) also appeared to have a higher degradation efficiency than others reported for the catalytic removal of OTC and CR, as presented in Table 3 [52–59]. The 2 wt% $Co_3O_4/TiO_2/GO$-1 photocatalyst exhibited negligible deactivation towards OTC degradation over five consecutive cycles (Fig. S8).
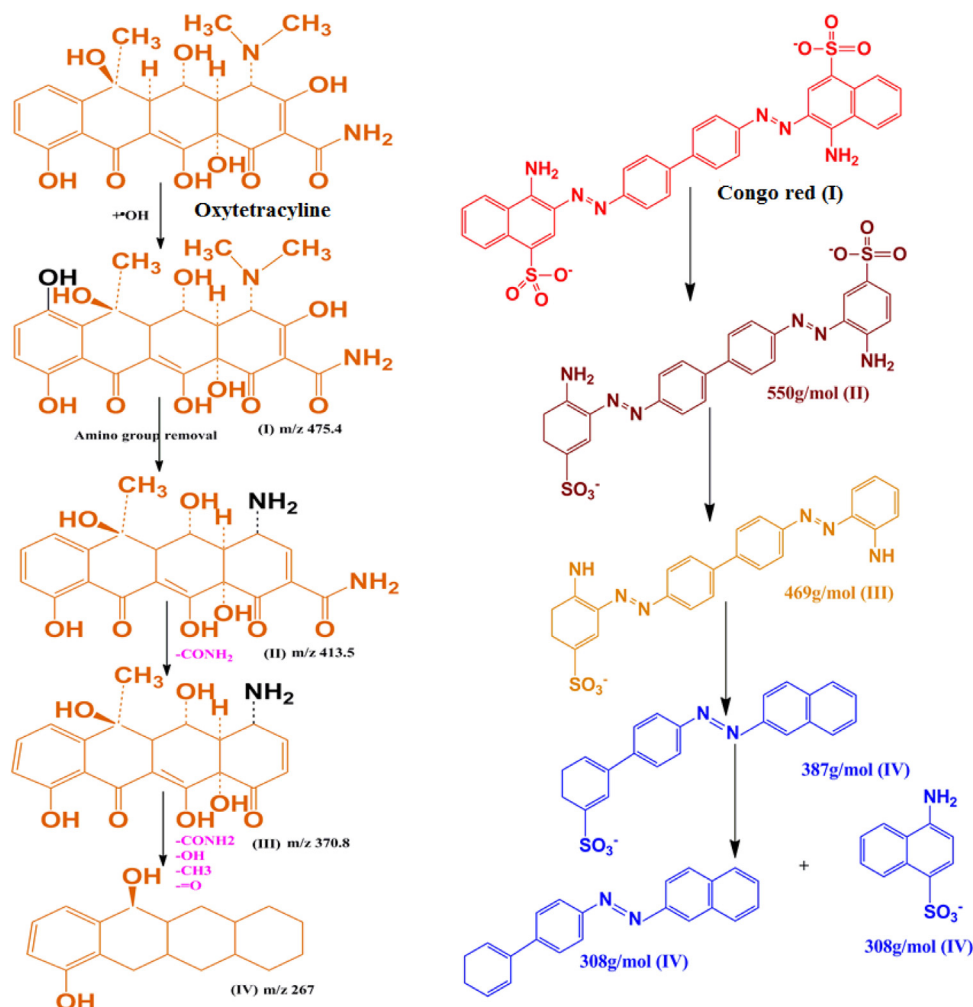
The photocatalytic degradation pathways for OTC and CR were subsequently investigated by LC–MS/MS as a function of reaction time (Fig. S9 and S10 respectively). A range of products were observed consistent with hydroxyl radical ($\bullet$OH) mechanisms

[58,60] involving stepwise hydroxylation (+16 Da), decarbonylation (−28 Da), demethylation (−14 Da) and dehydration (−18 Da) as illustrated in Scheme 1.

Confirmation of the critical role played by radicals in OTC and CR degradation was obtained through the use of radical scavengers, specifically isopropyl alcohol (IPA), 1,4-benzoquinone (BQ), and ammonium oxalate (AO) to quench OH$\bullet$ radicals, superoxide radical anions ($O_2^{\bullet-}$) and holes (h^+) [39,51]. Fig. 7 shows the degradation efficiency of the 2 wt% $Co_3O_4/TiO_2/GO$-1 composite photocatalyst towards OTC and CR, which reveals a striking suppression in the presence of AO, indicating that holes are the primary active species for both pollutants, with OH$\bullet$ and superoxide radicals likely of secondary importance in photodegradation. Hydroxyl

Table 3
CR and OTC photodegradation over different photocatalysts.

Pollutant	Photocatalyst	Light source	[Pollutant]	[Catalyst]	% Removal	Time	Refs.
CR	P25 TiO$_2$	W 300W	40 mg/L	1.0 g/L	~90	210	[52]
CR	CS/n-CdS	Xe 300 W	20 mg/L	1.5 g/L	86	180	[53]
CR	Fe/CMS-1	UV 15 W	100 mg$/L	1.0 g/L	100	180	[54]
CR	Fe$_3$O$_4$@SiO$_2$ @TiO$_2$@MIP	UV + Microwave	30 mg/L	0.03 g/L	93	300	[56]
CR	Co$_3$O$_4$/TiO$_2$/GO	Xe 300 W	10 mg/L	0.25 g/L	91	90	This work
OTC	Photolysis	Hg 500 W	10 mg/L	–	95	240	[57]
OTC	Ti-MCM-41	Hg 100 W	50 mg/L	1 g/L	87	180	[58]
OTC	Graphene/TiO$_2$/ZSM-5	Visible 300 W	10 mg/L	0.2 g/L	100	180	[59]
OTC	Co$_3$O$_4$/TiO$_2$/GO	Xe 300 W	10 mg/L	0.25 g/L	91	90	This work

Scheme 1. Proposed reaction mechanism for the photocatalytic degradation of OTC and CR under simulated solar irradiation over 2 wt% $Co_3O_4/TiO_2/GO$-1.

radical formation was also examined by fluorescence spectroscopy using 2-hydroxy terephthalic acid (2-HTA) as a probe molecule (Fig. S11) in which the high fluorescence intensity for the composite evidences significant hydroxyl radical generation during the photodegradation process, and consequent suppressed charge recombination with respect to both the 2 wt% Co_3O_4/TiO_2 and single oxide phases.

3.9. Photoelectrochemical properties

In order to better understand the origin of the superior photocatalytic performance of the binary and ternary composites relative to pure titania and Co_3O_4, their photocurrent responses were investigated under pulsed simulated solar irradiation experiments as shown in Fig. 8. Photocurrents for both composites were
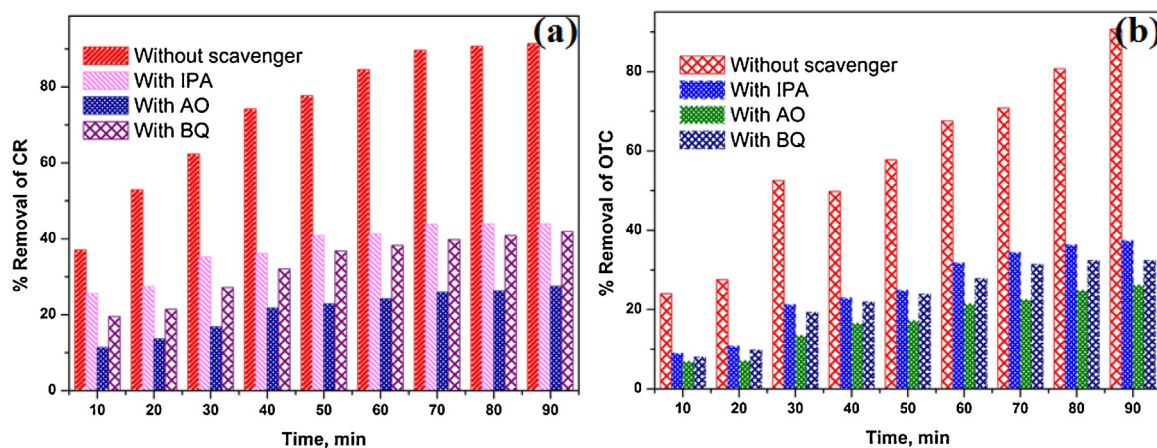

Fig. 7. Effect of radical scavenger addition on photodegradation of (a) CR and (b) OTC under simulated solar irradiation over 2 wt% $Co_3O_4/TiO_2/GO$-1 nanocomposite determined by UV–Vis.
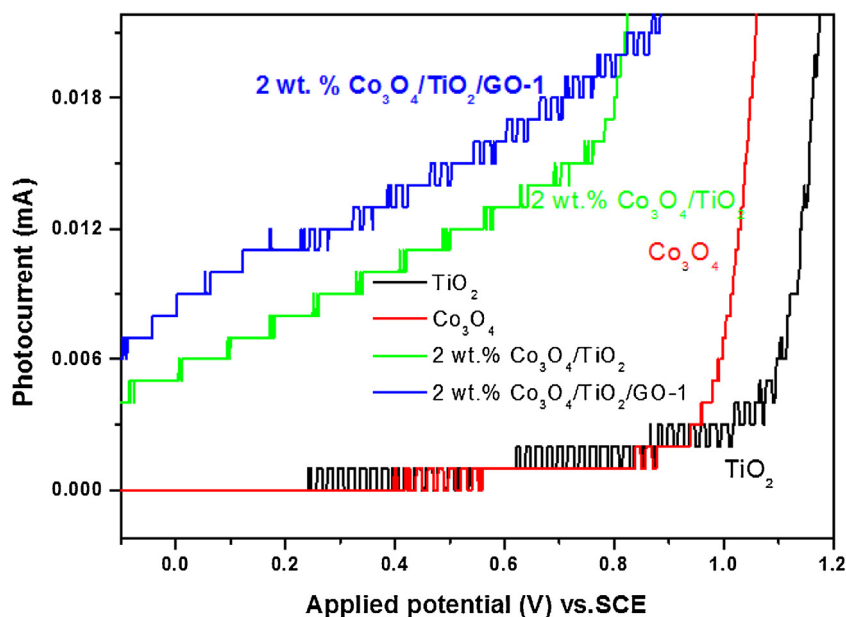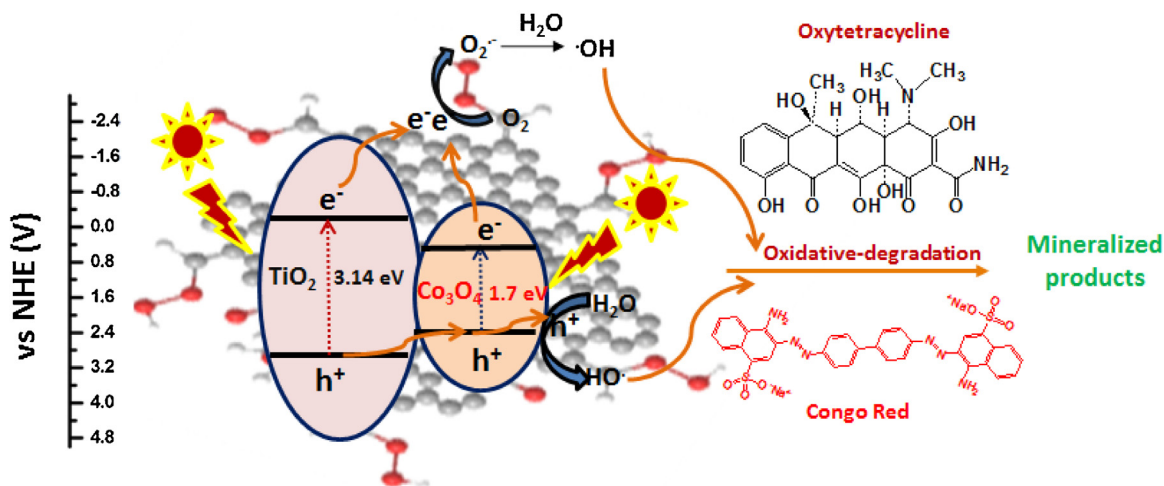
Fig. 8. Photocurrent response under simulated solar irradation of 2 wt% Co_3O_4/TiO_2, 2 wt% $Co_3O_4/TiO_2/GO-1$ and TiO_2 and Co_3O_4 references.

Scheme 2. Proposed mechanism for the photocatalytic degradation of organic pollutants by $Co_3O_4/TiO_2/GO$ nanocomposite.

approximately 15 times greater than the individual metal oxides at low bias (<1 V), indicating they exhibit significantly enhanced quantum yields.

3.10. Proposed mechanism

On the basis of the preceding results, we propose that CR and OTC photodegradation over the most active 2 wt% $Co_3O_4/TiO_2/GO-1$ composite photocatalyst occurs via the separation and transfer of photoinduced electron-hole pairs at the heterojunction interface of Co_3O_4 and TiO_2 [61] in contact with GO sheets as shown in Scheme 2. The valence band edge of p-type Co_3O_4 (E_{VB} = +2.5 eV vs. NHE) is more negative than that of n-type TiO_2 (E_{VB} = +2.77 eV vs. NHE) [62,63], and hence under visible light irradiation, electrons photoexcited into the CB of Co_3O_4 may be transferred into the CB of TiO_2. Residual holes within the Co_3O_4 VB may then either directly, or mediated through water oxidation to hydroxyl radicals, in turn photooxidize CR and OTC. UV photos may also excite electrons from TiO_2 CB to VB, with the resulting photoinduced holes transferred into the Co_3O_4 VB of through the heterojunction. Photoexcited

electrons in the CB of both Co_3O_4 and TiO_2 may be trapped in the LUMO of GO [64], thereby suppressing charge carrier recombination, in line with photocurrent and OH• trapping measurements. Photooxidation by holes appears the primary pathway for CR and OTC degradation.

4. Conclusions

Co_3O_4/TiO_2 and amine functionalized 2 wt% $Co_3O_4/TiO_2/GO$ nanocomposites were synthesized by sol-gel and hydrothermal routes, and comprised titania nanoparticles contacted with discrete Co_3O_4 and GO phases. Heterojunction formation between a low concentration of discrete Co_3O_4 nanoparticles and anatase titania strongly promoted the photocatalytic oxidative degradation of OTC and CR, which was further enhanced upon trace GO addition, likely the result of improved photoinduced charge-separation and associated hydroxyl radical formation as evidenced by trapping studies. Binary and ternary nanocomposites both exhibited superior quantum yields and lower recombination rates than pure Co_3O_4 or anatase. Amine functionalized 2 wt% $Co_3O_4/TiO_2/GO-1$

exhibits excellent rates and stability towards OTC and CR photodegradation under visible light irradiation.

Acknowledgments

Appendix A. Supplementary data

Supplementary data associated with this article can be found, in the online version, at http://dx.doi.org/10.1016/j.apcatb.2016.08.022.

References

[1] J.L. White, M.F. Baruch, J.E. Pander Iii, Y. Hu, I.C. Fortmeyer, J.E. Park, T. Zhang, K. Liao, J. Gu, Y. Yan, T.W. Shaw, E. Abelev, A.B. Bocarsly, Light-driven heterogeneous reduction of carbon dioxide: photocatalysts and photoelectrodes, chemical reviews, Am. Chem. Soc. (2015) 12888–12935.
[2] J. Liu, H. Bai, Y. Wang, Z. Liu, X. Zhang, D.D. Sun, Adv. Funct. Mater. 20 (2010) 4175–4181.
[3] D.L. Ashford, M.K. Gish, A.K. Vannucci, M.K. Brennaman, J.L. Templeton, J.M. Papanikolas, T.J. Meyer, Chem. Rev. 115 (2015) 13006–13049.
[4] E. Ioannidou, A. Ioannidi, Z. Frontistis, M. Antonopoulou, C. Tselios, D. Tsikritzis, I. Konstantinou, S. Kennou, D.I. Kondarides, D. Mantzavinos, Appl. Catal. B: Environ. 188 (2016) 65–76.
[5] J. Schneider, M. Matsuoka, M. Takeuchi, J. Zhang, Y. Horiuchi, M. Anpo, D.W. Bahnemann, Chem. Rev. 114 (2014) 9919–9986.
[6] R. Asahi, T. Morikawa, H. Irie, T. Ohwaki, Chem. Rev. 114 (2014) 9824–9852.
[7] M. Pelaez, N.T. Nolan, S.C. Pillai, M.K. Seery, P. Falaras, A.G. Kontos, P.S.M. Dunlop, J.W.J. Hamilton, J.A. Byrne, K. O'Shea, M.H. Entezari, D.D. Dionysiou, Appl. Catal. B: Environ. 125 (2012) 331–349.
[8] M. Liu, X. Qiu, M. Miyauchi, K. Hashimoto, J. Am. Chem. Soc. 135 (2013) 10064–10072.
[9] S.T. Kochuveedu, Y.H. Jang, D.H. Kim, Chem. Soc. Rev. 42 (2013) 8467–8493.
[10] A. Iwase, Y.H. Ng, Y. Ishiguro, A. Kudo, R. Amal, J. Am. Chem. Soc. 133 (2011) 11054–11057.
[11] L.-L. Tan, W.-J. Ong, S.-P. Chai, A.R. Mohamed, Appl. Catal. B: Environ. 166–167 (2015) 251–259.
[12] F. Zhang, A. Yamakata, K. Maeda, Y. Moriya, T. Takata, J. Kubota, K. Teshima, S. Oishi, K. Domen, J. Am. Chem. Soc. 134 (2012) 8348–8351.
[13] J. Lee, D.H.K. Jackson, T. Li, R.E. Winans, J.A. Dumesic, T.F. Kuech, G.W. Huber, Energy Environ. Sci. 7 (2014) 1657–1660.
[14] H. Yu, H. Irie, Y. Shimodaira, Y. Hosogi, Y. Kuroda, M. Miyauchi, K. Hashimoto, J. Phys. Chem. C 114 (2010) 16481–16487.
[15] Y.-S. Chen, P.V. Kamat, J. Am. Chem. Soc. 136 (2014) 6075–6082.
[16] M. Wang, J. Ioccozia, L. Sun, C. Lin, Z. Lin, Energy Environ. Sci. 7 (2014) 2182–2202.
[17] M. Liu, R. Inde, M. Nishikawa, X. Qiu, D. Atarashi, E. Sakai, Y. Nosaka, K. Hashimoto, M. Miyauchi, ACS Nano 8 (2014) 7229–7238.
[18] H. Yu, H. Irie, K. Hashimoto, J. Am. Chem. Soc. 132 (2010) 6898–6899.
[19] Y. Qu, X. Duan, Chem. Soc. Rev. 42 (2013) 2568–2580.
[20] S. Bala, I. Mondal, A. Goswami, U. Pal, R. Mondal, J. Mater. Chem. A 3 (2015) 20288–20296.
[21] S. Kumar, C.M.A. Parlett, M.A. Isaacs, D.V. Jowett, R.E. Douthwaite, M.C.R. Cockett, A.F. lee, Appl. Catal. B: Environ. 189 (2016) 226–232.
[22] H. Fei, J. Dong, M.J. Arellano-Jimenez, G. Ye, N. Dong Kim, E.L.G. Samuel, Z. Peng, Z. Zhu, F. Qin, J. Bao, M.J. Yacaman, P.M. Ajayan, D. Chen, J.M. Tour, Nat. Commun. 6 (2015).
[23] T. Wang, X. Meng, G. Liu, K. Chang, P. Li, Q. Kang, L. Liu, M. Li, S. Ouyang, J. Ye, J. Mater. Chem. A 3 (2015) 9491–9501.
[24] M. Zhang, M. de Respinis, H. Frei, Nat. Chem. 6 (2014) 362–367.
[25] E. Bi, H. Chen, X. Yang, W. Peng, M. Gratzel, L. Han, Energy Environ. Sci. 7 (2014) 2637–2641.
[26] D. Venieri, A. Fraggedaki, M. Kostadima, E. Chatzisymeon, V. Binas, A. Zachopoulos, G. Kiriakidis, D. Mantzavinos, Appl. Catal. B: Environ. 154–155 (2014) 93–101.
[27] J. Ran, J. Zhang, J. Yu, M. Jaroniec, S.Z. Qiao, Chem. Soc. Rev. 43 (2014) 7787–7812.
[28] T. Xiong, W. Cen, Y. Zhang, F. Dong, ACS Catal. 6 (2016) 2462–2472.
[29] A. Sharma, B.-K. Lee, J. Environ. Manage. 165 (2016) 1–10.
[30] N. Zhang, Y.-J. Xu, CrystEngComm 18 (2016) 24–37.
[31] N. Zhang, Y. Zhang, Y.-J. Xu, Nanoscale 4 (2012) 5792–5813.
[32] Y. Zhang, Z.-R. Tang, X. Fu, Y.-J. Xu, ACS Nano 4 (2010) 7303–7314.
[33] A.M.S. Solano, S. Garcia-Segura, C.A. Martínez-Huitle, E. Brillas, Appl. Catal. B: Environ. 168–169 (2015) 559–571.
[34] C. Zhao, M. Pelaez, X. Duan, H. Deng, K. O'Shea, D. Fatta-Kassinos, D.D. Dionysiou, Appl. Catal. B: Environ. 134–135 (2013) 83–92.
[35] D. Yang, A. Velamakanni, G. Bozoklu, S. Park, M. Stoller, R.D. Piner, S. Stankovich, I. Jung, D.A. Field, C.A. Ventrice Jr., R.S. Ruoff, Carbon 47 (2009) 145–152.
[36] B.D. Viezbicke, S. Patel, B.E. Davis, D.P. Birnie, Physica Status Solidi (b) 252 (2015) 1700–1710.
[37] H. Lin, C.P. Huang, W. Li, C. Ni, S.I. Shah, Y.-H. Tseng, Appl. Catal. B: Environ. 68 (2006) 1–11.
[38] S. Kumar, A. Baruah, S. Tonda, B. Kumar, V. Shanker, B. Sreedhar, Nanoscale 6 (2014) 4830–4842.
[39] W.-K. Jo, T. Sivakumar Natarajan, ACS Appl. Mater. Interfaces 7 (2015) 17138–17154.
[40] Q. Dai, J. Tang, Nanoscale 5 (2013) 7512–7519.
[41] P. Shi, R. Su, S. Zhu, M. Zhu, D. Li, S. Xu, J. Hazard. Mater. 229–230 (2012) 331–339.
[42] J.S. Lee, K.H. You, C.B. Park, Adv. Mater. 24 (2012) 1084–1088.
[43] N. Zhang, M.-Q. Yang, S. Liu, Y. Sun, Y.-J. Xu, Chem. Rev. 115 (2015) 10307–10377.
[44] D.O. Scanlon, C.W. Dunnill, J. Buckeridge, S.A. Shevlin, A.J. Logsdail, S.M. Woodley, C.R.A. Catlow, M.J. Powell, R.G. Palgrave, I.P. Parkin, G.W. Watson, T.W. Keal, P. Sherwood, A. Walsh, A.A. Sokol, Nat. Mater. 12 (2013) 798–801.
[45] R. Bansal, J. Bonnet, F. Stoeckli, Active Carbon, Marcell Dekker, 1988, New York and Bansel.
[46] S. Karthikeyan, D.D. Dionysiou, A.F. Lee, S. Suvitha, P. Maharaja, K. Wilson, G. Sekaran, Catal. Sci. Technol. 6 (2016) 530–544.
[47] M.C. Biesinger, B.P. Payne, A.P. Grosvenor, L.W.M. Lau, A.R. Gerson, R.S.C. Smart, Appl. Surf. Sci. 257 (2011) 2717–2730.
[48] S. Karthikeyan, R. Boopathy, G. Sekaran, J. Colloid Interface Sci. 448 (2015) 163–174.
[49] C. Botas, P. Álvarez, C. Blanco, R. Santamaría, M. Granda, P. Ares, F. Rodríguez-Reinoso, R. Menéndez, Carbon 50 (2012) 275–282.
[50] Y. Miao, Z. Zhai, L. Jiang, Y. Shi, Z. Yan, D. Duan, K. Zhen, J. Wang, Powder Technol. 266 (2014) 365–371.
[51] W.-K. Jo, T.S. Natarajan, Chem. Eng. J. 281 (2015) 549–565.
[52] H.-x. Guo, K.-l. Lin, Z.-s. Zheng, F.-b. Xiao, S.-x. Li, Dyes Pigm. 92 (2012) 1278–1284.
[53] H. Zhu, R. Jiang, L. Xiao, Y. Chang, Y. Guan, X. Li, G. Zeng, J. Hazard. Mater. 169 (2009) 933–940.
[54] J. Gong, K. Yao, J. Liu, Z. Jiang, X. Chen, X. Wen, E. Mijowska, N. Tian, T. Tang, J. Mater. Chem. A 1 (2013) 5247–5255.
[55] X. Liu, D. Xu, D. Zhang, G. Zhang, L. Zhang, Appl. Catal. B: Environ. 186 (2016) 193–203.
[56] S. Wei, X. Hu, H. Liu, Q. Wang, C. He, J. Hazard. Mater. 294 (2015) 168–176.
[57] S. Jiao, S. Zheng, D. Yin, L. Wang, L. Chen, J. Environ. Sci. 20 (2008) 806–813.
[58] H. Chen, Y.-P. Peng, K.-F. Chen, C.-H. Lai, Y.-C. Lin, J. Environ. Sci. 44 (2016) 76–87.
[59] X.-Y. Hu, K. Zhou, B.-Y. Chen, C.-T. Chang, Appl. Surf. Sci. 362 (2016) 329–334.
[60] Y. Liu, X. He, Y. Fu, D.D. Dionysiou, J. Hazard. Mater. 305 (2016) 229–239.
[61] D.B. Hamal, K.J. Klabunde, J. Phys. Chem. C 115 (2011) 17359–17367.
[62] Y.Q. Liang, Z.D. Cui, S.L. Zhu, Z.Y. Li, X.J. Yang, Y.J. Chen, J.M. Ma, Nanoscale 5 (2013) 10916–10926.
[63] S. Berardi, S. Drouet, L. Francas, C. Gimbert-Surinach, M. Guttentag, C. Richmond, T. Stoll, A. Llobet, Chem. Soc. Rev. 43 (2014) 7501–7519.
[64] F. Dong, H. Wang, Z. Wu, J. Phys. Chem. C 113 (2009) 16717–16723.